Characteristics of small protoplanetary disc warps in kinematic observations

Alison K. Young,[1,2,3]⋆ Richard Alexander[1], Giovanni Rosotti[1,4] and Christophe Pinte[5]

[1]*School of Physics and Astronomy, University of Leicester, University Road, Leicester, LE1 7RH, UK.*
[2]*SUPA, Institute for Astronomy, University of Edinburgh, Blackford Hill, Edinburgh, EH9 3HJ, UK.*
[3]*Centre for Exoplanet Science, University of Edinburgh, Edinburgh, EH9 3HJ, UK.*
[4]*Leiden Observatory, Leiden University, P.O. Box 9513, 2300 RA Leiden, the Netherlands.*
[5]*Monash Centre for Astrophysics (MoCA) and School of Physics and Astronomy, Monash University, Clayton, Vic 3800, Australia.*

ABSTRACT

Many circumstellar discs appear to have misaligned central regions that give rise to shadows seen in scattered light observations. Small warps ($< 20°$ misalignment) are probably more common but are also more difficult to detect than the large misalignments studied previously. We present the characteristics of CO emission that may be used to identify a small disc warp, found from synthetic ^{13}CO maps of a model misaligned circumbinary disc. The spectra are not symmetrical, so fitting a Keplerian model is not appropriate and can hide a warp or lead to spurious features such as spirals appearing in the residuals. We quantify the observed warp structure by fitting sinusoids to concentric annuli of the disc. From this we can trace the radial variation of the peak velocity and of the azimuth of the peak velocity, i.e., the twist. At near face-on inclinations, these radial profiles reveal the warp structure. The twist remains detectable at moderate inclinations ($i_{\text{outer disc}} \lesssim 35°$) in the absence of radial flows but the measured inclination must be accurate to $\lesssim 5°$ to allow detection of the radial variation. The observed twist does not provide a direct measure of the warp structure because of its dependence on optical depth. The warp causes broad asymmetries in the channel maps that span several channels and that are distinct from localised features caused by embedded planets and gravitational instability. We suspect that kinematic evidence of warps may have been missed and we suggest a few examples where the data may be revisited.

Key words: hydrodynamics – line:profiles – protoplanetary discs – radiative transfer

1 INTRODUCTION

Planets are thought to form in the dusty gas discs around protostars. Many questions remain on how exactly planet formation takes place and the evolution of protoplanetary discs is far from well understood. Protoplanetary discs are a by-product of star formation and, since most stars form in multiple systems, circumbinary discs are likely to be common. The conservation of angular momentum of the infalling gas leads to the formation of an accretion disc around the central star(s). In the simplest, and probably most common, case, the angular momentum vectors of the star(s) and disc are parallel. The disc evolves viscously and there is no out-of-plane motion, aside from internal motion of the gas within the disc due to turbulence for example and any disc winds.

Theoretical work has demonstrated that if the orbital plane of a binary is misaligned with respect to its circumbinary disc, gravitational torques can warp and tear the disc (Terquem & Bertout 1993; Papaloizou & Terquem 1995; Fragner & Nelson 2010; Nixon et al. 2013). Protoplanetary discs are assumed to evolve viscously, with accretion driven by the outward transport of angular momentum by viscous torques. The origin of this angular momentum transport is

assumed to be turbulence, which is parameterised as a viscosity, α_{SS} (Shakura & Sunyaev 1973). A perturbing force such as that of a misaligned binary may drive a warp, which propagates in the disc. The disc viscosity determines how the warp propagates. In thin, viscous discs where the disc viscosity exceeds the aspect ratio, $\alpha_{\text{SS}} > h/r$, the warp propagates diffusively (Papaloizou & Pringle 1983). For protoplanetary discs, $\alpha_{\text{SS}} < h/r$ and a warp propagates via bending waves (Papaloizou & Lin 1995; Lubow & Ogilvie 2000). Protoplanetary discs are most likely to fall in the latter regime since their turbulence is generally very low (Flaherty et al. 2015; de Juan Ovelar et al. 2016; Flaherty et al. 2020). Current understanding of accretion mechanisms in protoplanetary discs is incomplete and we note that disc accretion may be wind driven (Lesur 2021). In this case, should the effective α_{SS} be even smaller, the disc would move further into the wavelike regime in which warps are still able to form.

The warp structure is similar whether it is caused by a perturbing star or planet, inside, outside of, or embedded within the disc. The shape of the warp is time-dependent and the exact structure of the perturbed disc depends on several factors. For a more massive perturbing companion and/or a larger misalignment between the disc and the orbit of the companion, the amplitude of the warp is greater. A greater warp amplitude can result in higher accretion rates and accretion flows onto the central star. The effective viscosity affects the communication timescale of the warp and a low viscosity may make

a disc susceptible to breaking or tearing. If the precession torque of the companion on the disc exceeds the internal torques, the disc breaks into distinct planes. The effects of such large misalignments are reasonably straightforward to detect.

Many protoplanetary discs which display out-of-plane structures have now been observed. Near infra red scattered light images of protoplanetary discs show a wide variety of shadows. Broad shadows may result from a warped region and/or an inner disc(s) with a slight inclination to the outer disc (e.g. HD 143006, Benisty et al. 2018; Pérez et al. 2018b; HD 139614, Muro-Arena et al. 2020; GW Orionis, Kraus et al. 2020). To cast narrow shadows across a disc requires a highly misaligned inner disc (e.g. HD 142527, Marino et al. 2015; HD 100452, Benisty et al. 2017). The difference between the orientation of an misaligned inner disc and outer disc is also clear in the observed velocity field from molecular line observations. A twisted first moment map is typically interpreted as evidence of a warp (Rosenfeld et al. 2012; Facchini et al. 2018; Zhu 2019) and the origin of the observed twist or 'S'-shape in the velocity centroids is explained by Casassus et al. (2015). A twisted velocity field, however, is also produced by fast radial flows and the two scenarios may be very difficult to distinguish (Rosenfeld et al. 2014). Radial flows occur when there is a high misalignment between the binary/planet and the disc. Several of these features have been observed in HD 142527 and were explained by the presence of a binary companion by Price et al. (2018b). The variability of the 'dipper' star AA Tau was well fit by a warped inner disc, suggesting that such variability is another indicator of a warp (Esau et al. 2014; Alencar et al. 2010).

The key motivation for the quantitative detection and measurement of warped protoplanetary discs is twofold. Firstly, in the case that the perturbing bodies are known and well-characterised, measurements of the warp provide an insight into the viscosity and thermal structure of the disc, since the warp is sensitive to those properties. Measurements of warped discs would therefore be invaluable for elucidating the hydrodynamical processes driving disc evolution. A second reason is simply that warps indicate a perturbation. For some systems, it may be possible to link a warp with a known stellar or sub-stellar companion. Otherwise, a warp may hint at a hidden planet (e.g. Nealon et al. 2018) or past stellar fly-by (e.g. Xiang-Gruess & Papaloizou 2013; Cuello et al. 2019). Various theoretical models (e.g. Terquem 2013; Xiang-Gruess & Papaloizou 2013; Nealon et al. 2018) have been used to examine the disc structures that would result from embedded planets of various masses and at various inclinations. While there is not a unique correlation between structure and planet, warp measurements are likely to prove useful to place constraints on the nature of possible planets and allow some scenarios to be ruled out.

Previous work to elucidate the observational characteristics of warped discs has tended to concentrate on those with large warps and broken discs. Juhász & Facchini (2017) studied simulated discs with initial misalignments of $15°$ and $30°$. Their findings include that warps cannot be detected with spatially unresolved spectra but resolved CO observations reveal brightness asymmetries and a twisted first moment map. Facchini et al. (2018) show that with an initial inclination of $60°$ between the binary and disc, the resulting broken disc is readily detectable.

The well–studied disc TW Hya shows signs of a small central misalignment (e.g. Roberge et al. 2005; Debes et al. 2017; van Boekel et al. 2017; Poteet et al. 2018) and the possibility of the confirmation of a small warp from kinematic observations is a motivation for this work. Typically, parametric models are fitted to observational kinematic data to derive the properties of a disc. We will also examine how well the CO line emission traces the intrinsic gas velocities. Given how common broad shadows seem to be in protoplanetary

discs, small warps are expected to be common. In this paper we use hydrodynamical and radiative transfer simulations to study discs with a central binary that is only slightly misaligned with respect to the disc. We identify the characteristics of small warps in synthetic CO emission maps and suggest a method for quantifying observations of warps. Velocity fields derived from synthetic observations via both the classic first moment method and the quadratic method of Teague & Foreman-Mackey (2018) are compared to the input model to better understand how the observed velocities relate to the intrinsic gas velocities of the source.

In section 2 we detail the methods for simulating the warped discs using hydrodynamical models and for generating the CO line maps with full radiative transfer. In 3, we present the synthetic CO observations of the simulated warped discs and describe the methods for analysing the them and comparing with the hydrodynamical models. We then examine how well the CO maps trace the intrinsic disc structure and the effects of viewing inclination, uncertainty in the source inclination and the optical depth on the derived warp structure. Finally, in section 4 we discuss the kinematic characteristics of small warps and the interpretation of line observations and provide the implications for identifying small protoplanetary disc warps.

2 NUMERICAL METHODS

2.1 Hydrodynamical simulations

Hydrodynamical modelling was performed with PHANTOM (Price et al. 2018a), a smoothed particle hydrodynamics (SPH) code that been used extensively to model disc warping and tearing (e.g. Lodato & Price 2010; Nixon et al. 2013; Nealon et al. 2018). While an embedded planet may arguably be the most exciting cause of warping in a protoplanetary disc, we opt to simulate a disc around a misaligned, circular equal mass binary. We would like to identify signatures of the small warp independently of any other structures. A circular binary allows us to study the disc kinematics as simply as possible, without a gap forming in the disc, a misaligned inner disc or a planet-induced spiral.

We consider an equal mass binary modelled with sink particles (Bate et al. 1995), which are free to accrete material from the disc. The sink particles are both 1 $M_\odot$, with semimajor axis $a = 1$ au and have an accretion radius of 0.1 au. The disc is modelled with 5×10^6 SPH particles and has an initial inner radius of $r_{in} = 2.2$ au and outer radius $r_{out} = 100$ au. The aspect ratio $h/r = 0.05$ at r_{in} and $h/r = 0.13$ at r_{out}. The surface density is initially axisymmetric and set via $\Sigma(r) = \Sigma_0 (r/r_{in})^{-p}$, where $\Sigma_0 = 14.3$ g cm^{-2} and $p = 0.5$. Self-gravity is not included so the disc mass has no effect on the evolution of the disc or of the binary. We use a locally isothermal equation of state with $c_s \propto r^{-0.25}$.

As discussed above, the waves excited by a perturbation (in this case, the torque from the misaligned binary) propagate via bending waves in protoplanetary discs. We therefore require to maintain $\alpha < h/r$ to maintain this regime as far as possible. The artificial numerical viscosity is set with $\beta_{AV} = 2$ and α_{AV} is varied with the switch of Cullen & Dehnen (2010) between 0.01 and 1.0. Additionally, we impose $\alpha_{SS} = 0.01$. Lower values of α_{SS} are posited for protoplanetary discs, however lower values can be modelled reliably only with much higher resolution because of the contribution of the numerical viscosity in SPH, which is resolution-dependent. For this work, we are concerned only with the observational appearance of small warps so it is inconsequential if the warp propagation is not always wavelike in the simulations.
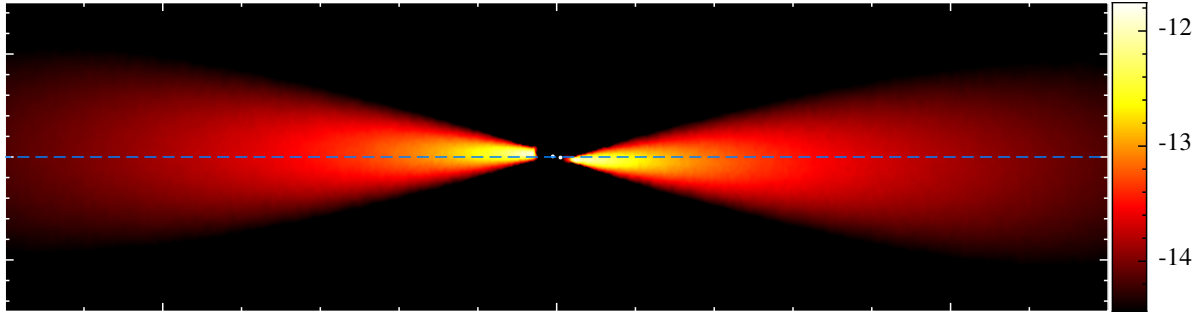
Figure 1. Density slice through the snapshot from the $10°$ binary inclination hydrodynamical simulation used for the analysis here. The colour bar gives the density scale in g cm^{-3} and the dashed line indicates the initial position of the disc midplane. The vertical extend of the image is 30 au and the horizontal extent is 70 au. The vertical scale is stretched to emphasize the warp. The positions of the central stars (sink particles) are indicated by the white points.

Three simulations are run with the binary initially inclined to the disc plane at an angle of 5, 10 and $20°$. Additionally, we run an 'aligned' simulation where the binary orbits in same plane as the disc for comparison. Snapshots are extracted after 1350 binary orbits (955 years) for analysis. The disc radial communication timescale is ~ 4600 yr (Lubow & Martin 2018). We extract the snapshot before the warp has propagated to the outer edge of the disc, preventing any erroneous reflections. The global precession time is found following the method described in Smallwood et al. (2019) (their Eq. 6) and is 15,000 yr. The alignment timescale is significantly shorter in simulations than analytical predictions due to the additional dissipation due to the numerical viscosity. Over the course of 1600 orbits the misalignment of the binary orbit and disc in the $10°$ binary inclination simulation decreases by less than $0.8°$ at 20 au and less than $0.4°$. Alignment of the disc to the binary orbital plane is not therefore not a significant factor to consider here.

2.2 Radiative transfer: synthetic line maps

The snapshots from the hydrodynamical simulations are read into a radiative transfer code, MCFOST (Pinte et al. 2006, 2009), to simulate CO line maps. A 3D Voronoi mesh is created from the SPH particle density values, which is then used for the temperature and line transfer calculations. The distance to the source is set to 140 pc. A uniform dust-to-gas ratio of 0.01 with dust grain sizes following a power law distribution $N \propto a^{-3.5}$, for grain sizes 0.03μm $< a < 1$ mm (Mathis et al. 1977). For the dust optical properties we use the 'smoothed astronomical silicate' model (Draine & Lee 1984; Laor & Draine 1993; Weingartner & Draine 2001). The stars each have a luminosity of 2.1 L$_\odot$, which was estimated from the 1Myr Siess isochrone (Siess et al. 2000). The dust temperatures were then calculated assuming radiative equilibrium.

CO molecular line emission was then calculated using the velocity data from the hydrodynamical simulation and assuming the dust and gas temperatures are equal. We assume local thermodynamic equilibrium. The line we choose to model, ^{13}CO, originates deep enough in the disc for this assumption to hold. The relative abundance of ^{13}CO is 1.3×10^{-6} (Woods & Willacy 2009). We implement an approximation for freeze out of CO, wherein the abundance is set to zero in regions where $T < 20$ K. In practice, this has little effect because only cells very close to the midplane are altered. The channel width is 50 ms^{-1}, which is the best spectral resolution feasible for interferometric observations of a protoplanetary disc. CO maps are also simulated with the disc density scaled by factors of 0.1 and 10 to provide an approximation of the effect of the disc opacity on the observed velocity.
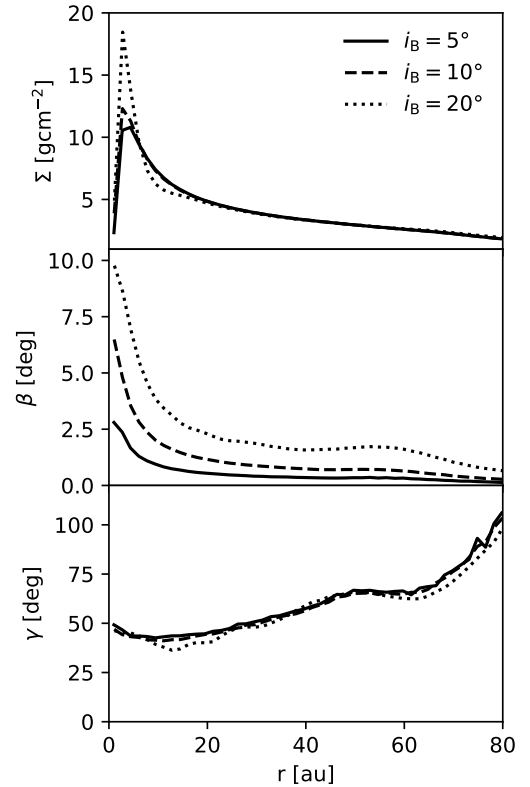

Figure 2. Surface density (Σ), tilt (β) and twist (γ) profiles at 1350 orbits for the three simulations with the binary inclined by 5, 10 and $20°$ with respect to the disc. The tilt differs between the models whereas the twist is similar for all three.

3 RESULTS

3.1 Hydrodynamical simulations

The disc is initially aligned with the x-y plane while the orbital plane of the binary is inclined with the ascending node located on the positive x-axis. Both the binary and disc rotation are anticlockwise. As the system evolves, a warp develops near to the inner disc boundary, deforming the centre of the disc out of the plane, and the wave propagates outwards. In the snapshots shown, the warp is oriented with the maximum extent away from the observer located $\sim 45°$ anticlockwise from the x-axis. The disc morphology can be seen in the

density slice from the 10° binary inclination simulation presented in Fig. 1.

The angular momentum unit vector varies radially in a warped disc. The unit vector of the specific angular momentum for a ring within the disc is $\hat{l} = (\cos\gamma\sin\beta, \sin\gamma\sin\beta, \cos\beta)$. Here two angles are defined, β and γ, which are respectively known as the tilt and twist. The tilt and twist describe the shape of the warped disc and represent the rotation relative to the z- and x- axes.

The disc surface density profile, $\Sigma(r)$, and angular momentum components tilt, β, and twist, γ, after 1350 binary orbits are plotted in Fig. 2. The disc surface density profile and twist are similar for all inclinations of the central binary but the tilt increases with binary inclination.

3.2 Comparison of velocity fields from the hydrodynamic simulation and CO maps

The raw velocity field is extracted from the hydrodynamical simulation output by calculating the density-weighted average z-component of the velocity, $\langle v_z \rangle$, looking along the z axis (the assumed line of sight here):

$$\langle v_z \rangle = \frac{\int \rho v_z dz}{\int \rho dz}. \tag{1}$$

The CO velocity maps are generated with BETTERMOMENTS (Teague & Foreman-Mackey 2018; Teague 2019a) from the velocity cubes. We use two methods to calculate the velocity field, the first moment map and the quadratic method of find the velocity of the peak of the spectrum, and compare the results obtained with each. The first moment map (intensity-weighted velocity) is calculated in the standard manner:

$$\langle v \rangle = \frac{\sum\limits_{i=1}^{N} I(v_i)v_i}{\sum\limits_{i=1}^{N} I(v_i)}, \tag{2}$$

where $I(v_i)$ is the flux density of velocity channel i. The peak velocity, v_{peak}, map is found by fitting a quadratic curve in velocity space to the pixels near the maximum value of the spectrum for each spatial increment in the image. The method is described in detail in Teague & Foreman-Mackey (2018).

We concentrate on ^{13}CO (3-2) emission, since this spectral line is commonly targeted in high-resolution submillimeter observations and will be included in the future exoALMA Large Program. Velocity maps were generated as described above for a face on ($i = 0°$) viewing inclination [1] of the outer disc and are shown in Fig. 3. These velocity maps amount to a perfect deprojection and Keplerian subtraction of a disc. They show the deviation from the velocity field expected from an unperturbed Keplerian disc observed at a low inclination. Observations of inclined discs will naturally be affected by the non-uniform optical depth along the line of sight across the disc and we will discuss the implications of this later. Qualitatively, these maps reveal a change in the orientation of the red- and blue-shifted sides with radius, not dissimilar to the appearance of a misaligned inner disc. There is a spiral tail-like feature at the outer edge of the warp wave. Similar structures are seen in the ^{13}CO maps to the raw

___

[1] Here we can define the inclination as the rotation of the model from the initial orientation. In observations the inclination may be uncertain since the orientation of the mid plane varies radially in a warped disc.

hydrodynamical density-weighted velocity field, $\langle v_z \rangle$. The velocity field appears noticeably more twisted in the v_{peak} map.

The residuals found when subtracting the SPH models' average velocity field $\langle v \rangle_{SPH}$ from the synthetic CO-derived velocity fields indicate that the observed velocity fields are not equal to the 'real' velocity field. There is a difference in the twist of the first moment and v_{peak} residuals and the warp appears slightly rotated in the v_{peak} map. We also see a new spiral feature appear in the residuals, which is most pronounced for the 20° binary inclination model. We emphasise that there is no embedded planet here, but such a feature could be mistaken for a planet-induced spiral arm.

3.3 Quantitative description of the kinematic structures

3.3.1 Analysis

So far, our interpretation of kinematics observations of putative warped discs goes little further than spotting the 'twist' which makes comparisons of different discs difficult. Next, we describe the method implemented to quantify the radial dependence of the peak projected velocity and of the observed 'twist'. We compare the velocity values at selected annuli centred on the image centre, which here is the centre of mass of the binary. After binning the pixels into the desired annuli, we fit a sine curve using CURVE_FIT from SCIPY.OPTIMIZE to the pixel azimuthal angles, ϕ, and line-of-sight velocity values, v_{los}, for each annulus:

$$v_{los} = v_{max}\sin\left(\phi + \theta_p\right). \tag{3}$$

An example of this fit is shown in appendix A. This approach is very similar to fitting an azimuthally averaged, projected rotation curve like method presented in Casassus & Pérez (2019). Here however, we fit selected radial ranges, rather than annuli covering the whole disc, and obtain two useful parameters. v_{max} is the amplitude or maximum value of v_{los}. In Fig. 3, we saw the distinct 'twist' which is already used as an observational indicator of warp structure. This twist is now quantified as θ_p, the phase angle of the peak velocity. We can now compare the variation of the peak velocity and phase angle with radius for various types of observation and disc structures.

3.3.2 Velocity and twist profiles

We extract velocity values for annuli at 6, 10, 12, 20, 30, 40 and 50 au, each within ±0.2 au. We present the velocity radial profiles v_{max} and phase angle θ_p variation for the three warped disc models in Fig. 4. The v_{max} gradients are steepest within $r \lesssim 20$ au, where the effect of the warp is greatest. The velocities remain < 1 km s^{-1} outside 10 au, which presents a challenge for observations. For the smallest warp (5° binary inclination) the difference in v_{max} at 50 and 10 au is ~ 0.1 km s^{-1} and would require very high spectral resolution to detect.

There is an offset of $\lesssim 30°$ between the phase angle measured from the simulation directly and from the synthetic first moment maps. For the v_{peak}-derived values this increases to $\lesssim 60°$. As we saw in Fig. 3, the phase angle changes slightly faster with radius for the CO-derived values, indicating a more twisted observed structure. The change in θ_p with radius is $\sim 40°$ between 20 and 50 au in the first moment map. The difference in θ_p from the v_{peak} maps depends on the initial binary inclination and is $\sim 30°$ for the 10° binary inclination model. This shift should easily be detectable in real observations. None of the observed θ_p profiles traces the sharp twist toward the centre of the disc that we see in the values measured directly from the simulation.
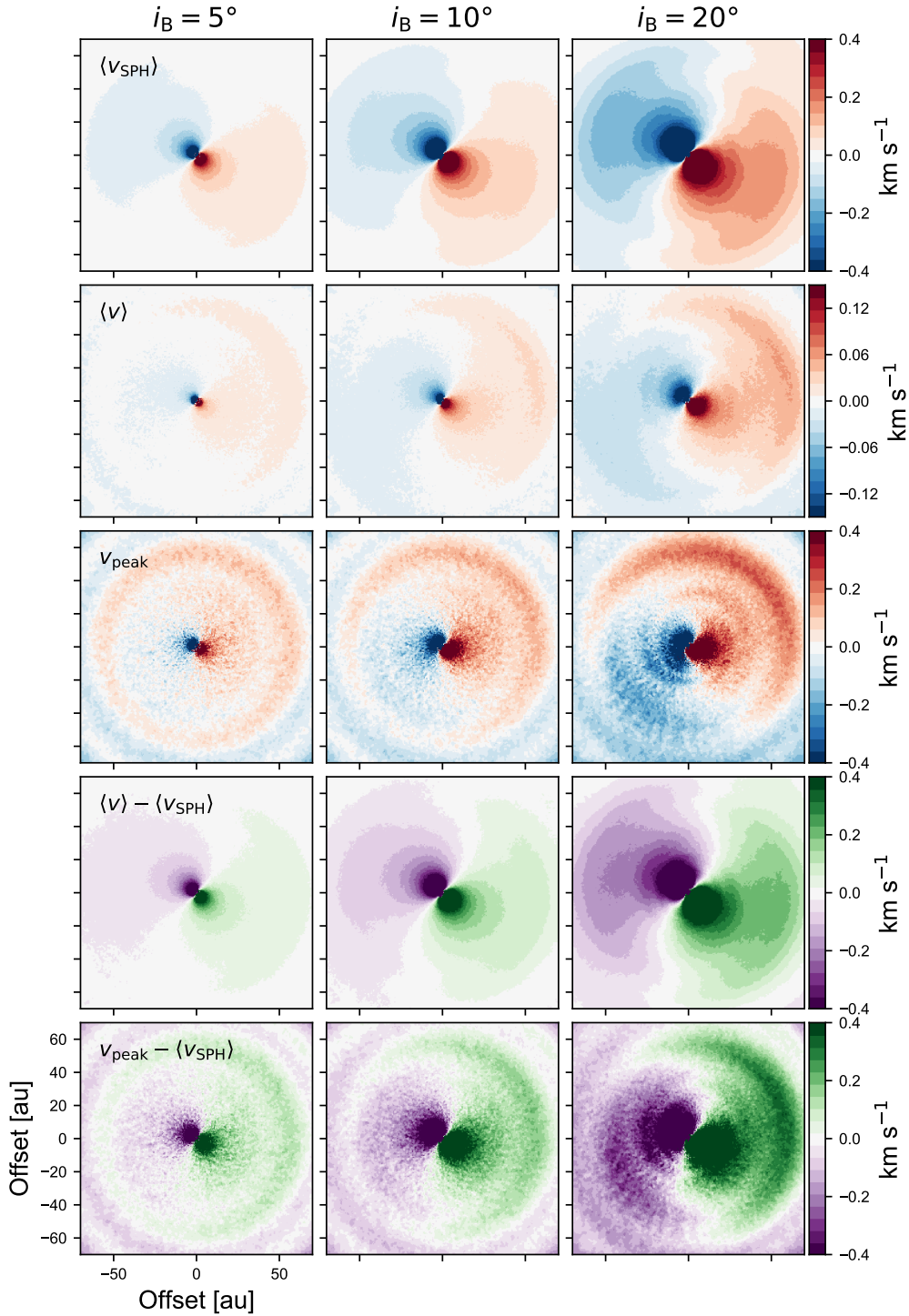
Figure 3. Velocities derived from the SPH model ($\langle v_{SPH} \rangle$, density-weighted column-averaged velocity), ^{13}CO 3-2 first moment maps, $\langle v \rangle$, and v_{peak} maps. The bottom two rows contain the residuals between the velocity fields derived from the synthetic CO maps and the raw SPH model. The columns are three simulations with the binary orbit inclined at 5, 10 and 20° to the disc after 1350 binary orbits. Note the different scale for the first moment maps since the observed velocities are much lower.

3.3.3 How well does CO trace the velocity structure?

In Fig. 4, the profiles extracted from synthetic CO maps are also compared to the velocity fields from the hydrodynamical simulations and this reveals how well the observationally-derived values represent the disc kinematics.

The velocity profiles obtained from the synthetic CO maps differ markedly from the simulation velocity profile. The velocities derived from the first moment maps are smaller than those in the simulation and this difference increases at small radii and the profile is closer to a $v \propto r^{-0.5}$ Keplerian profile. The v_{peak}-derived velocities are much closer to the density-weighted velocities from the simulation and follow the gradient more closely. We recall how the velocity values are calculated from the hydrodynamical file and image data cubes (section 3.2) to explain these differences. The average z-velocity calculated from the hydrodynamic simulation directly in Eq. 1 is the average value of v_z in the $\hat{z}$ direction, weighted by the mass through the density, ρ. This is similar to the definition of the first moment map (Eq. 2), in which the velocity channels are weighted by the flux intensity. The residuals in Fig. 3 are greater for the v_{peak} map in places although the fitted values of v_{max} from the v_{peak} map are closer to the SPH values. This is due to the azimuthal offset of v_{max} between the v_{peak} map and SPH velocity field, which increases with radius (see Fig. 4, bottom right panel).

The line profiles across a warped disc are not symmetrical, as would be the case for a face-on, unwarped disc. Spectra for regions across the disc in the $10°$ binary inclination model viewed face-on are shown in Fig. 5. In many regions of the disc the peak is shifted from $v = 0$ but there is also a 'shoulder' on one side of the peak in some panels. The first moment average will therefore not coincide with the peak of the spectrum but will drag the average velocity towards zero. Even when the asymmetry of the spectrum is slight, the velocity deviations we need to detect are < 0.5 km s^{-1}. Therefore, assuming a symmetrical spectral profile introduces a significant error. In protoplanetary discs, the CO lines are optically thick so the emission traces the velocity structure at the $\tau \approx 1$ surface. Analytical descriptions of warped discs implement a thin disc approximation in which the angular momentum unit vector $\hat{L}$ is constant in each cylindrical annulus. Due to the curve of the disc midplane, $\hat{L} = \hat{L}(r)$ and $\hat{L}$ for similar radii are not parallel (see Fig. 6). Therefore, the projected velocity $v_{\text{los}} = v_{z'}(z')$ (where z' is the distance along the line of sight) and the depth of the emission surface in a thick disc becomes relevant. The question of whether the CO emission accurately traces the velocity structure in the disc therefore becomes more complex. For the purposes of comparing observations with simulations, the v_{peak} map matches the simulation projected velocities more closely because the peak is not reduced by the averaging. The higher values will be easier to detect and show up more structure.

3.4 Effect of optical depth

The projected velocity of a warped disc is not constant along the line of sight, as discussed earlier. Consequently, emission originating from different optical depths can be expected to give different values of projected velocity for the same spatial position. We simulate ^{13}CO 3-2 emission maps scaling the disc surface density by factors of 0.1 and 10 in addition to the original value as a proxy for discs of differing the optical thickness. The resulting radial profiles of v_{max} and θ_p can be found in Fig. 7.

The first moment maps, again, underestimate the velocity and phase angle in all cases. The lower the surface density, and the more optically thin the disc is, the closer the observationally derived values

are to the those from the SPH simulation. This can be understood simply because a greater column of gas is contributing to the total emission due to the reduced effect of self-absorption. The SPH mass-weighted column-averaged velocity can be thought of as the perfectly optically-thin limit. The magnitude of the peak velocity derived from the v_{peak} maps decreases with increasing opacity, although the values are closer to the simulation values than the values derived from first moment maps.

The phase angle of the warp has a greater shift relative to the SPH model with increasing opacity. For both methods of deriving the velocity, the 10Σ model has a substantially greater change in θ_p with radius than the SPH model. This indicates that the opacity of a disc has a major contribution to the appearance of twisted velocity structures. This is an important result to consider because it means a distorted disc may appear more twisted than it really is if observed with an optically thick tracer.

3.5 Detectability in an inclined disc

The main challenge with detecting a small warp is that velocity deviations are likely to be smaller than the line of sight velocity due to the disc rotation at most inclinations. We extract the radial maximum velocity and warp phase angle profiles from spectral cubes produced from viewing the $10°$ binary inclination warped disc at inclinations up to $35°$. The same analysis is repeated with the unperturbed aligned disc to look for differences due to the warp. The velocity maps were first deprojected spatially such that the disc appears circular but the velocity values were unchanged and not Keplerian subtracted.

The profiles are shown in Fig. 8. The differences in v_{max} between the warped and aligned discs are very small outside of 10 au with even a slight inclination. The change in θ_p with radius is far smaller when the disc is viewed at an inclination. This change is only a few degrees between 20-50 au but any deviation from a flat profile, i.e. a twist, is indicative of a warp. The detection of a warp in this manner is therefore only limited by the noise and spatial resolution of the data. The greatest deviations are seen where the warp is strongest, in this case at $r < 20$ au, so the focus needs to be on observations suited to that scale for the best chance of detection.

3.6 The effect of deprojection errors on warp characterisation

As observational methods are increasingly capable of measuring velocities to ~ 30 m s^{-1} precision, the derived gas velocities are susceptible to the effects of systematic errors in inclination and position angle which are generally only known to the nearest $\sim 5°$. These errors will introduce an additional velocity field in the same way as an additional inclination. Fig. 9 includes the radial v_z and θ_p profiles for viewing inclinations 1, 2, and $5°$, which is equivalent to an error in deprojection by the same value (in i, assuming the position angle is accurate).

The velocity profile for a circumbinary disc in which the orbital planes of the binary and disc are aligned are plotted for comparison in Fig. 9 for a small viewing inclination. When viewed face-on, the velocity profile of the warped disc differs most from the linear profile of the aligned disc but this flattens off with increasing inclination. With a $5°$ error in inclination, a warp of this amplitude is likely to be missed. The greatest deviations are seen in the inner 20 au in v_{peak}, with velocities exceeding 0.5 km s^{-1}. Pinning down the velocities in the inner regions of the disc where the warp amplitude is greater is therefore important so it may be worthwhile compromising the spectral resolution slightly to achieve greater spatial resolution.
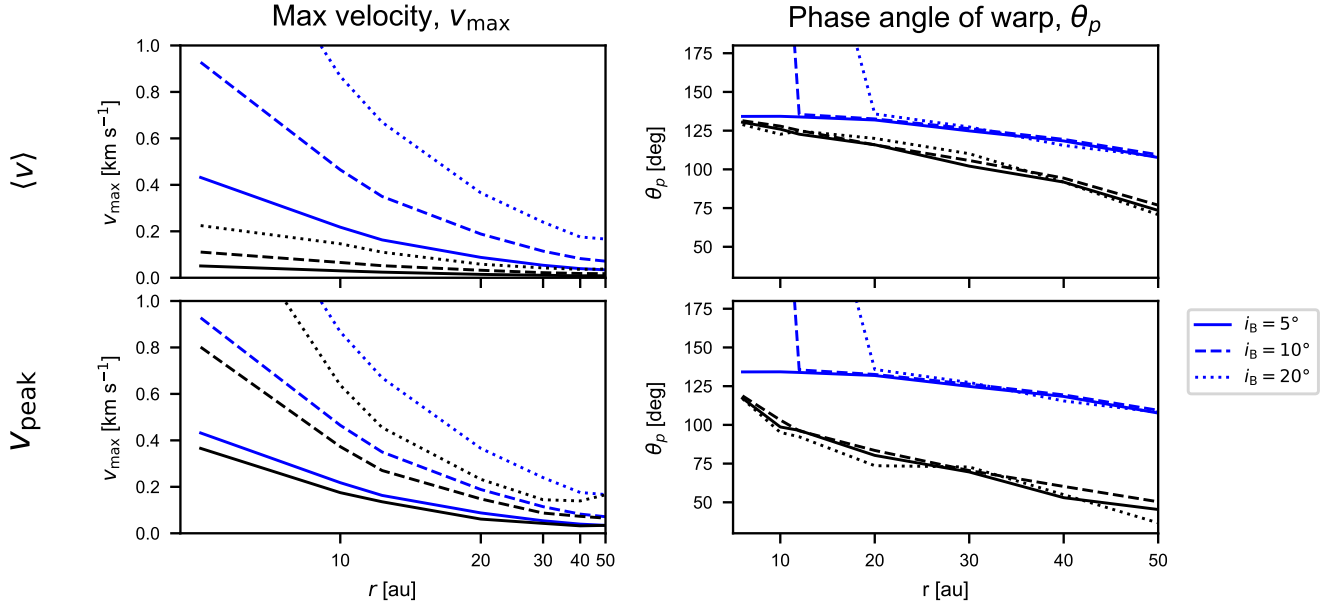
Figure 4. v_{max} and θ_p profiles for models with initial misalignments of 5, 10 and 20° of the binary to the disc after 1350 orbits. The profiles in the top row were derived from first moment maps and the profiles in the bottom row were derived from v_{peak} maps. Blue lines indicate results from the SPH output and black lines are results derived from the simulated ^{13}CO maps.

The presence of a warp is most clearly seen in the 'twist', or variation of θ_p with radius (Fig. 9). At a viewing inclination $i = 5°$, for $20 < r < 50$ au the change $\Delta\theta_p$ is $\sim 5°$ which is likely to come close to the uncertainty due to noise in the data. If radii down to 10 au are available, $\Delta\theta_p$ increases to nearly 15°. If the section of the disc where the warp amplitude is greatest is observed, then small warps should be readily detectable if the error in deprojection is no greater than $\sim 5°$.

The appearance of the warp is affected by its azimuthal position in the disc. In Fig. 10, we demonstrate the appearance of a warp with just a 1° error in the inclination used for deprojection at four azimuthal positions relative to the assumed line of nodes. Just by eye, there is an apparent difference in both the velocity profile and the twist. Indeed, the radial profiles in Fig. 11 for $i = 1°$ confirm this. For a 270° position, the twist produced by the warp is imperceptible. For a more detailed study of this effect, the reader is referred to Juhász & Facchini (2017).

inclination, a difference in offset of the emission of a central velocity channel may be detectable between opposite sides of the disc. Emission from the reverse side of the disc is faintly visible towards the top of the image. The channel map in panel (f) is from the velocity cube for which the v_{peak} map in Fig. 10 and the change in θ_p (Fig. 11) showed little evidence of a twist. Nevertheless, the channel map is asymmetrical, revealing the warp. Panel (g) shows the asymmetries between positive and negative velocity channels for the same disc.

These asymmetries are seen for small warps even at a moderate viewing inclination and therefore provides a method for detecting small warps when it is not possible to discern them from the velocity maps due to the viewing inclination. In addition, it is likely that this approach will not require as high velocity resolution because the effect is not limited to a narrow range of channels. The asymmetries extend over tens of au, equivalent to multiple synthesized beam widths with ALMA. Consequently, the observed structures should be robust against noise.

3.7 Channel maps

Examining the channel maps can reveal small deviations from a smooth Keplerian rotation profile that would otherwise have gone undetected. We find asymmetries in the emission across several channels. In Fig. 12, selected channel maps produced for the 10° binary inclination model viewed at various inclinations are presented alongside the corresponding channel from the aligned disc model. In Fig. 12 (a) the red-shifted emission crosses over onto the opposite side of the disc at the centre. Similarly, in panel (b) the blue-shifted emission crosses to the opposite side, but only for the far side of the disc. Panel (c) shows a brightness asymmetry and the emission from the near and far side is offset from each other. In panel (d) emission from the lower surface of the disc is faintly visible in the warped disc but not in the aligned disc. Panel (e) shows that, even at a moderate

3.8 The effects of noise and spatial resolution

The results we have presented so far are derived from idealised noise-free synthetic observations. We now demonstrate that the observational characteristics of small warps that we described are recoverable with a representative spatial resolution and signal to noise ratio. The issues of image fidelity when imaging interferometric data are known difficulties to observers. The methods used to mitigate these problems will depend on a number of factors to do with the specific observation. For this reason, we consider a generic case as an example. We add thermal noise to the data and convolve with an 0.1 arcsec Gaussian beam to emulate representative quality of data. We compare the results obtained from the synthetic line emission calculated for a distance of 140 pc and from the same synthetic data but with the flux scaled for a distance of 60 pc, the approximate distance to TW
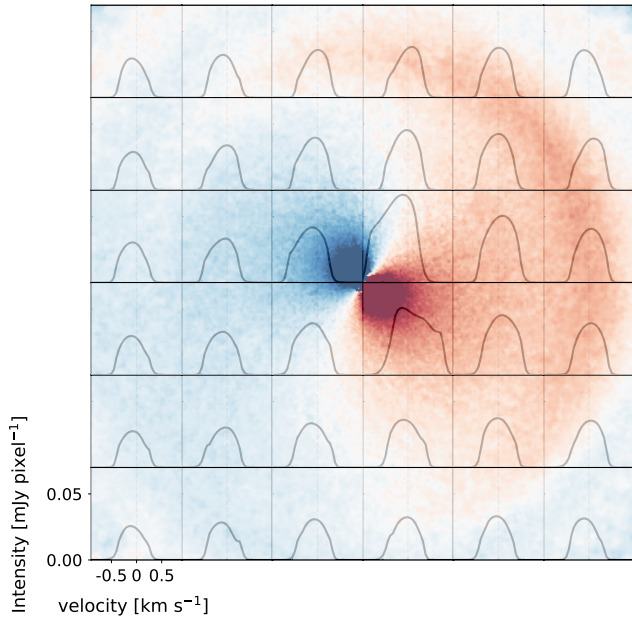
Figure 5. Spectra extracted from the central pixel of panels across the face-on ^{13}CO 3-2 spectral cube for the 10° binary inclination model after 1350 orbits and viewed face-on. Each panel is 0.17 × 0.17" (∼ 24 × 24 au). The spectra do not have Gaussian profiles, meaning the assumption of a Gaussian for deriving the velocity will lead to errors. In the background is the first moment map for the same cube, showing the region of the disc represented by each panel.
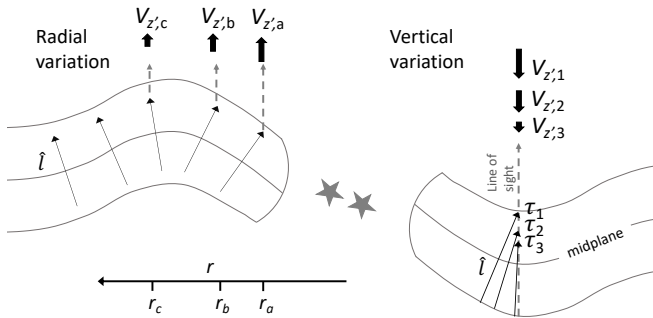

Figure 6. Sketch diagram to explain the observed CO velocities. The left hand side illustrates the radial variation of the line-of-sight velocity $v_{z'}$ at r_a, r_b and r_c. The right hand side shows the vertical variation of $v_{z'}$, which will be evident in tracers of differing optical depths τ_i. The gas velocity is perpendicular to $\hat{l}$, the local specific angular momentum unit vector. Thin arrows indicate the orientation of $\hat{l}$ and solid arrows indicate the magnitude of the observed tangential velocity. The angular momentum vector becomes more aligned with the the line of sight deeper into the disc. Shallower layers therefore have a greater tangential velocity and greater line-of-sight velocity.

Hydrae. At 60 pc, the flux density in the warped region of the disc is ∼ 220 mJy beam^{-1} and at 140 pc is ∼ 40 mJy beam^{-1}, where the beam size is 1 arcsec. Gaussian noise was added with $\sigma = 6.2$ mJy and $\sigma = 17$ mJy, representing the sensitivity of the ALMA 12 m array at a spectral resolution of 0.05 km s^{-1} for a 4 hour and 30 minute integration respectively. In creating the velocity maps with BETTERMOMENTS, the velocity was smoothed over 5 channels. The

velocity maps were calculated for between ±4.0 km s^{-1} for $i = 5°$ and between ±10.0 km s^{-1} for $i = 35°$ to reduce the effect of noise.

The derived velocity and twist profiles from the convolved data for the 10° binary inclination at viewing inclinations of 5° and 35° are compared with the idealised results presented earlier in Fig. 13. At a distance of 140 pc, the beam size is 14 au which means that the velocity structure is not resolved in the inner regions and the derived values from the convolved velocity maps deviate from the idealised model. At $r > 20$ au, where the disc is adequately resolved, the v_{peak}-derived velocity profile follows the idealised model closely. The same is true of the twist profile at $i = 35°$ but at $i = 5°$ we see an increased twist. The velocity and twist derived from the first moment maps suffer most from noise and poorer resolution. From this, it is clear that better quality data is obtained from the peak velocity maps.

For the both distances and integration times, the maximum velocity profile is recovered reasonably well from the v_{peak} maps where the disc is resolved. In contrast, the phase angle profile is sensitive to noise and the finite resolution. The width of the annuli chosen for extracting the phase angle is a trade-off between averaging out noise and being narrow enough to resolve the change in phase angle with radius, noting that the twist cannot be extracted on scales smaller than the beam size. Given these issues, the methods of analysis presented here are more suited to nearer protoplanetary discs, unless a more distant disc happens to be particularly extended and bright in CO. In the scenario presented here, the twist does not show up in the v_{peak} map at $i = 35°$ even for the 60 pc disc, indicating that lack of evidence of a twist does not necessarily discount the presence of a warp.

4 DISCUSSION

4.1 Comparisons to related work

Identifying small warps kinematically is naturally challenging because the velocity perturbation is small. Nevertheless, we have identified three kinematic signatures of slightly warped protoplanetary discs. The radial profile of the projected velocity deviates from the expected near-Keplerian profile, becoming much steeper in the warped region. By fitting a sinusoid to the azimuthal velocity profiles for concentric annuli we can quantify the twist and this will facilitate direct comparisons between discs. Lastly, individual channel maps present various asymmetries and distortions, even at a moderate inclination of 35°. Depending on the viewing inclination, not all of these effects may be observed.

Previous theoretical work to determine the observability of non-axisymmetric structures such as circumplanetary discs and planet-induced wakes usually implements a fitting of a rotation curve to the whole disc (e.g. Rosenfeld et al. 2013; Pinte et al. 2018b; Pérez et al. 2018a; Teague et al. 2019b). This method works well when there is a consistent inclination throughout the disc but for a warped disc, the velocity field is twisted and the projected radial velocity profile deviates from that of a Keplerian disc. The position angle and inclination vary with radius which means that these parameters cannot be consistently fit for the whole disc. For the purposes of deprojection, it might be better to estimate these values for the outer disc from continuum observations. Casassus & Pérez (2019) implement a method which accounts for radial variation in inclination and position angle and also fits for the height of the emitting layer in the disc. In this paper, we also fit annuli extracted from the disc rather than the whole disc. This approach is better suited for warped discs, since pixels in a given annulus correspond to regions of the disc
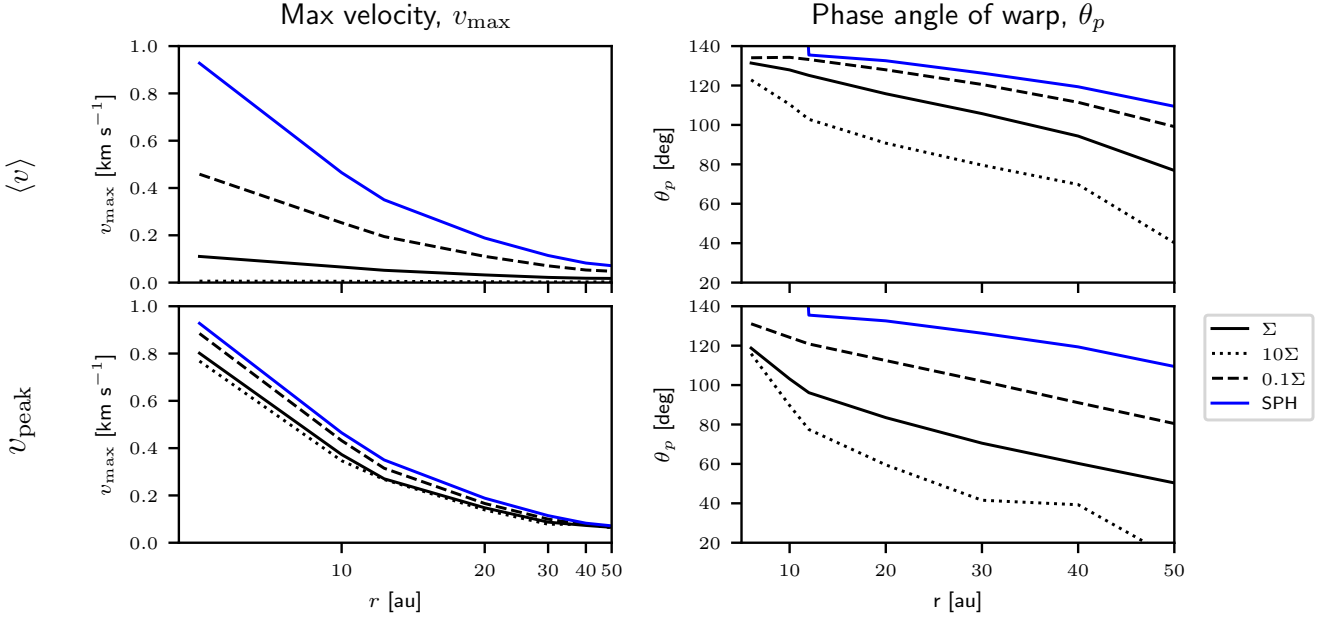
Figure 7. Effect of optical depth/surface density. $v_{\max}$ and θ_p profiles as for Fig. 9 for the same disc model. The profiles were derived from simulated ^{13}CO 3-2 line emission but with the surface density scaled by factors of 10 and 0.1 (10Σ and 0.1Σ).
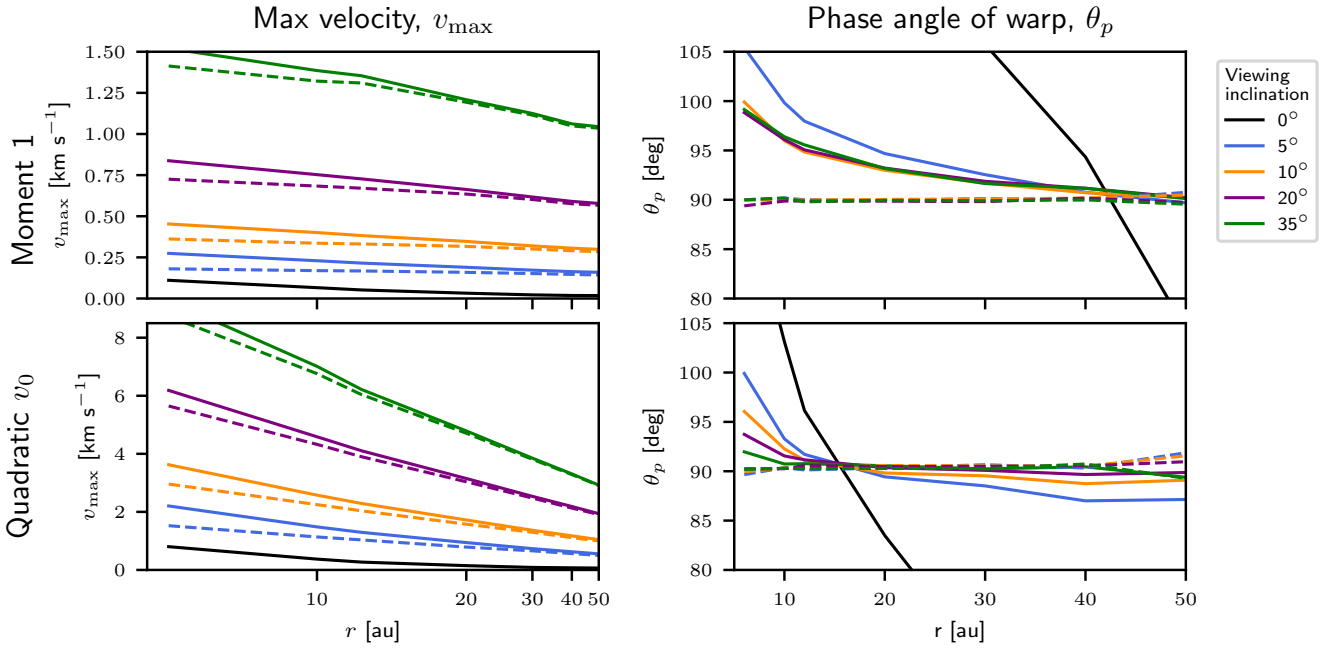

Figure 8. The velocity and warp phase angle measurement when disc is viewed at an inclination for the 10° binary inclination warped disc (solid lines) and the unwarped aligned disc (dashed lines). The velocity maps were spatially deprojected first but no Keplerian subtraction is applied.

with similar orientations. We do not look to measure the absolute orientation of the annuli, but rather the differences between them to obtain a quantitative measure of the twist.

Resolved kinematic observations or protoplanetary discs typically consider the height of the emitting gas layer (e.g. Pinte et al. 2018a; Casassus & Pérez 2019) to map the rotation profile more accurately,

accounting for the fact that protoplanetary discs are not razor thin. The height of the $\tau = 1$ surface in a warped disc is a complex shape. Any analytical z/r profile would not be accurate and would not improve the accuracy of the results so we do not consider this here.
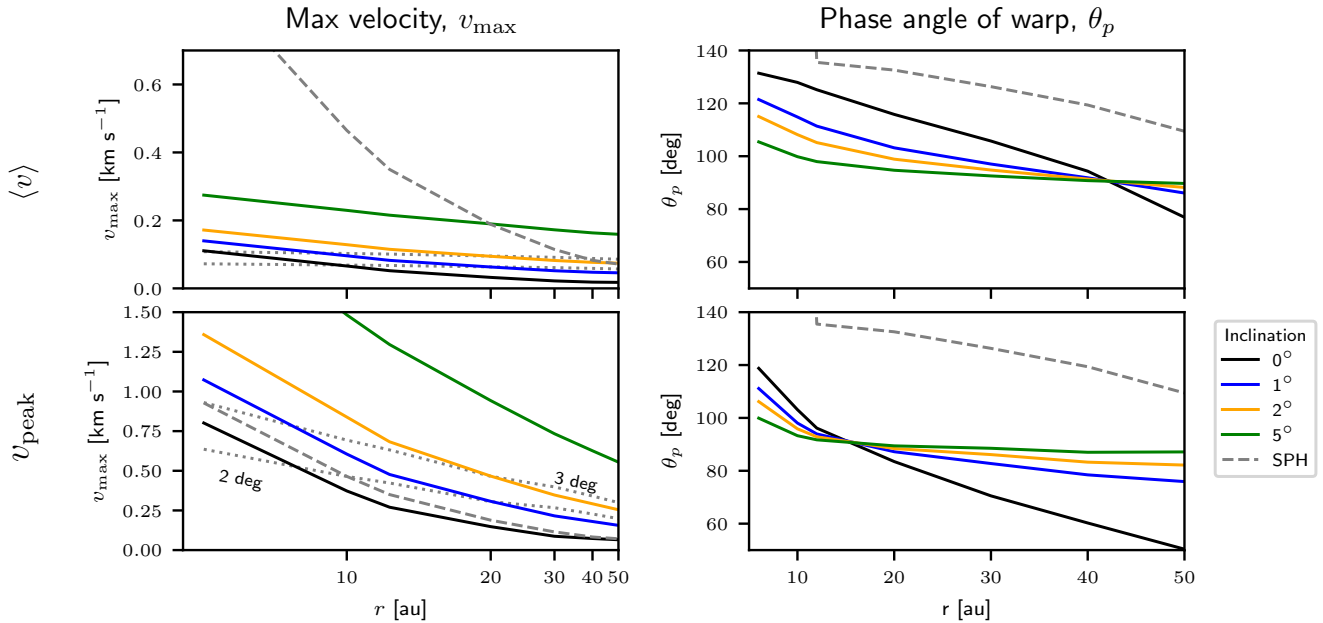
Figure 9. Fitted v_{max} and θ_p profiles from inclined velocity maps, equivalent to small errors in the inclination used for deprojection. Note the different vertical scales in the left column. The labeled dotted lines show the velocity profiles for the aligned circumbinary disc viewed at 2 and 3° for comparison.

4.2 Sources of uncertainty

Ideally, we would like to measure the velocity structure of a warped disc. The out-of-plane gas motions are easily detected when the disc is viewed face-on, but are swamped by the rotation and quickly become indistinguishable with just a few degrees inclination. An important question is how closely the observed velocity field follows the source velocity field. We have shown that the velocity field obtained from first moment maps differs significantly from the source gas velocities. This is because the average obtained from the first moment is only valid if the spectrum is symmetrical, which is not true for a warped disc. The quadratic method of calculating v_{peak} of Teague & Foreman-Mackey (2018) recovers the model structure more accurately but there will be some dependence on the optical depth of the tracer.

The methods employed above for deriving the radial profiles of projected velocity and phase angle of the warp (twist) assume that the deprojection of the disc observation is perfect. The inclination and position angle is difficult to constrain and is rarely constrained to better than a few degrees accuracy. The most accurate way of estimating these values is by fitting Keplerian disc models to the observations. This is a problem when we are dealing with a disc that is not flat. There have been attempts to produce analytical models of warped discs for the purpose of fitting observations, however this introduces more free parameters to describe the shape of the warp and the analytical disc model does not always replicate the morphology seen in hydrodynamical simulations. Brief testing of fitting simulated CO observations with EDDY (Teague 2019b, see Appendix B) showed that no good fit could be obtained for warped discs that were close to face on and for inclined warped discs the central mass tended to be overestimated or the fitted centre of the disc was offset from the true centre. The resulting model-subtracted images often showed spiral features, presumably a product of the poor fitting. The fitting was improved by masking out the warped region but this naturally

requires some prior knowledge and the results can be sensitive to the selected region. If there is a clear twist in the inner regions and a large enough near-Keplerian region of the disc beyond, this method may perform more accurately. It may also be possible to mask out channels close to zero since for lower velocities the perturbation due to a warp is a larger fraction of total. When the velocity map appears non-Keplerian, this kind of fitting is naturally unsuitable and we must rely upon continuum imaging to estimate the inclination and position angle.

We expect that the disc inclination may only be known to within 5° and have shown that this error in deprojection can conceal the kinematic signatures of small warps. The error serves to flatten the projected velocity profile which makes it less distinct from that of a smooth near-Keplerian disc and also reduces the observed twist. For small warps, the deprojection needs to be accurate to ∼ 5° or better to reliably pick up the kinematics, so this uncertainty is a major limitation. We have shown that velocity perturbations caused by small warps can be discerned in the continuum-subtracted channel maps, which avoids the need for deprojection.

Supposing the orientation of the warp in the disc and the disc on the sky are well constrained, we estimate that the velocity measured from the ^{13}CO v_{peak} map is within 0.1 km/s or around 25 per cent of the true mean gas velocity for the case studied here. Differences in the optical depth are expected to have a smaller effect on the observed velocity since we saw a change in the v_{peak} profile of > 0.1 km s^{-1} with a factor 100 change in the disc surface density. The disc appears more twisted with increased opacity which means we cannot take the warp morphology at face value. An optically thin tracer is necessary to recover the true morphology of the warp. Before we can consider linking the observed disc structure to its physical properties and those of the perturbers, we need to be aware of these limitations and of the resulting uncertainties or find ways to mitigate them.

At moderate inclinations, any radial flows will contribute to the radial velocity and twist profiles. The twist due to the warp has a
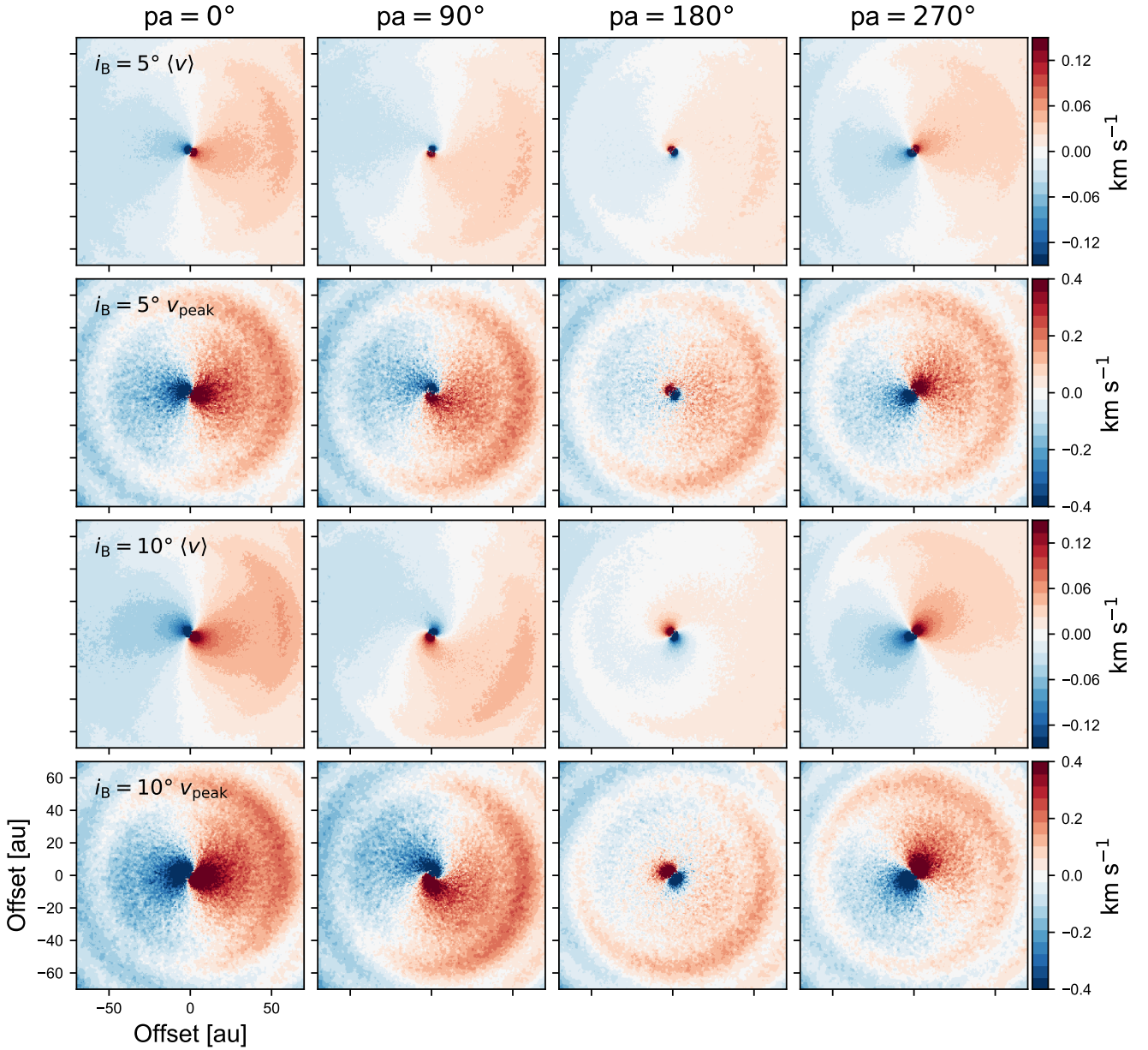
Figure 10. The effect of warp position in the disc. ^{13}CO first moment and v_{peak} maps for the 5° and 10° binary inclination models viewed at an inclination of 1° with the warp rotated to four different position angles. The clarity of the 'twist' is variable becoming barely discernible in some cases.

greater phase angle at low inclinations. The component of the projected velocity that is due to radial flows increases with inclination. This means that at near-face on inclinations, any radial flows would have a negligible contribution to the radial velocity and twist profiles, compared to that of the warp. At moderate inclinations, however, the possible presence of radial flows is an additional caveat.

We showed in section 3.8 that a representative spatial resolution and thermal noise can change the observed twist at low inclinations. Crucially, there is still a detectable change in phase angle and the maximum velocity profile derived from the convolved v_{peak} map reproduces the idealised profile where the disc is resolved, despite the noise and reduced resolution.

4.3 Are we missing warps or misinterpreting them?

The prevalence of broad shadows in scattered light images of protoplanetary suggests that misalignments are common but a pronounced twist in the velocity field is currently the primary method of identifying a warp. Additionally, given the prevalence of binary and higher order multiple systems, as well as the somewhat chaotic nature of the accretion onto protostellar discs, for example in the models of Bate (2018), we would expect warps to be common. This raises the question of why more warped discs have not been identified. Perhaps we are missing them due to the methods used to analyse kinematic data or perhaps the signatures of warps are misinterpreted or discounted.

As discussed earlier, many methods of analysing disc kinematics assume that the spectrum is Gaussian, or at least symmetrical. This conceals the velocity deviations due to the warp and gives a
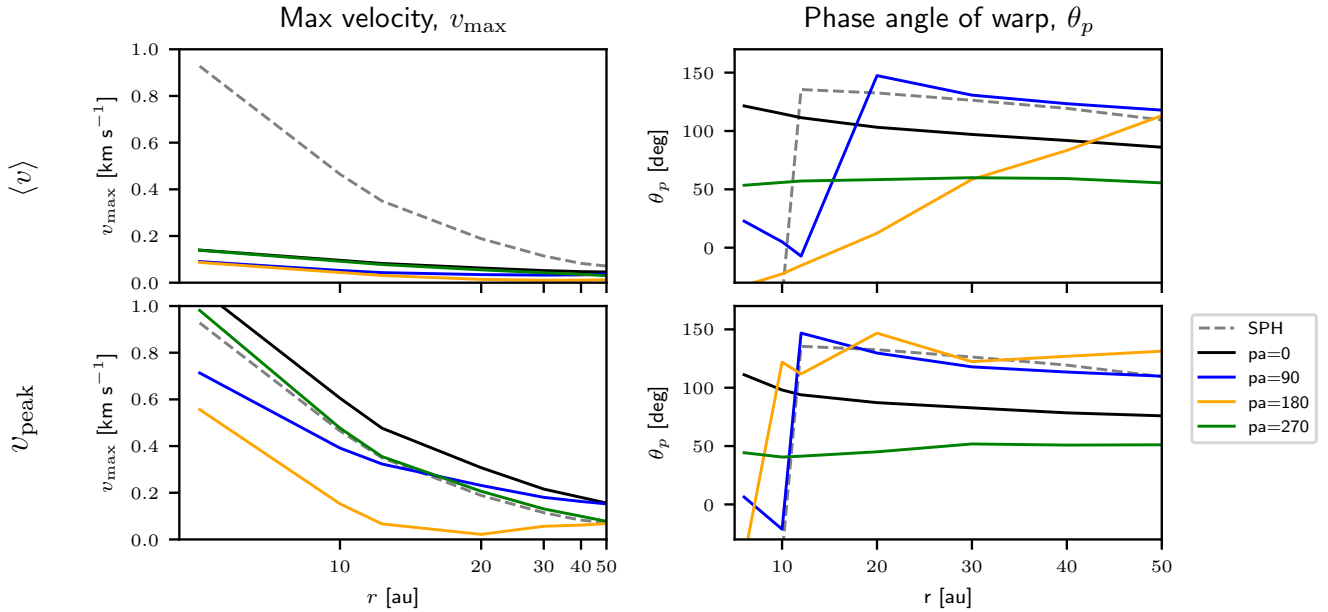
Figure 11. Dependence on position angle of warp in disc. v_{max} and θ_p profiles as for Fig. 9 for the same disc model. The profiles were derived from simulated ^{13}CO 3-2 line emission for a viewing inclination of 1° with the disc first rotated such that the warp is at a different position angle.

misleading velocity field in the first moment map. Attempts to fit a Keplerian disc model will give incorrect results. This may lead to a warp going unnoticed. If a Keplerian model is fitted and subtracted, the resulting residuals may show spurious spiral arm features rather than an obvious warp.

The velocity deviation is a small fraction of the rotation velocity so will be tricky to detect above this background. We base most of the analysis here on the deprojected observed disc and have examined how the derived warp properties are affected by small errors in the inclination. If we can observe the region of the disc that is warped at high angular resolution then the maximum velocity profile can still be observed to be steeper than that of an unwarped disc. In the model here, the region were the warping is strongest is within $r < 20$ au and the velocity and twist profile are likely to be difficult to distinguish from that of an unwarped disc outside this region, depending on the noise and uncertainty in the maximum value of the velocities. The scales explored here is determined by the binary separation of 1 au. Small warps with larger angular size will of course be easier to resolve spatially. The implication here is that a warp could well be missed if observed at a spatial resolution too low to resolve the warped region. The asymmetries in the channel maps are small so it is possible that they would be missed if one is not looking for them. If there is no obvious twist in the observed velocity field, perhaps until now there would be no reason to look for evidence in the channel maps.

Depending on the azimuthal position of the warp, the twist may not be evident. We have seen, as also found by Juhász & Facchini (2017) and Facchini et al. (2018), that the relative positions of the line of nodes and the phase angle of the warp maximum determines whether the maximum perturbation is visible or not, and consequently determines the observed velocity profile. In these cases, the perturbation can still be seen in the channel maps.

Radial infall within a cavity gives similar twist and channel maps. Complementary submillimetre continuum imaging will con-

firm whether there is a central cavity and scattered light images will reveal shadows due to misalignments. Currently, these are the only features that may distinguish the two scenarios.

Another possibility is that small warps are being misinterpreted as other structures. Embedded planets can also cause velocity deviations (e.g. Perez et al. 2015; Teague et al. 2018; Pinte et al. 2018b). These are, however, very much localised, occurring in just one velocity channel and confined to a small region of the disc near the planet. The observed velocity field of a warped disc is also distinct from that of a gravitationally unstable disc with a spiral structure. In such discs we expect to see a finger-like structure in the first moment map protruding from the red-shifted side into the blue-shifted side of the disc (Hall et al. 2020) and the velocity perturbations are coincident with spiral arms. In a warped disc, there may be finger-like perturbations in the velocity map, outside of the central twisted region, but these are not coincident with spiral arms in the gas density.

The vertical shear instability can produce ring structures in line-of-sight velocity maps (Barraza-Alfaro et al. 2021) with a wiggle-like effect around the disc's line of nodes which bear some resemblance to the velocity maps we present for warped discs and have a similar magnitude. The key difference is that a warped disc has a twisted inner region whereas the vertical shear instability leaves a symmetrical velocity field in the inner disc and axisymmetric rings in the first moment map.

When there is a planet embedded in the disc, other perturbations can occur such as meridional flows (e.g. Teague et al. 2019a; Casassus et al. 2021). Care should be taken for regions that are close to a gap in the disc or a cavity because additional perturbations may be contributing to the velocity field.

4.4 Possible shallow warped discs from the literature

The effect of a small warp on the kinematic observations is subtle and we propose that many protoplanetary discs may be warped but
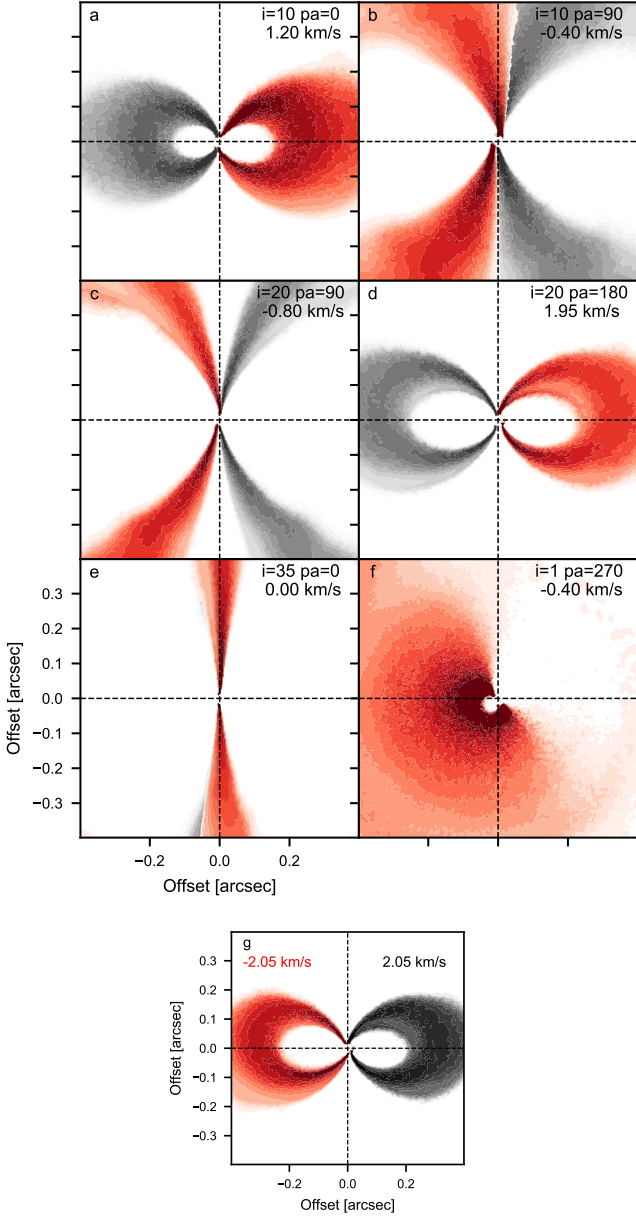
4.4.1 TW Hydrae

The suggestion that the centre of the TW Hya disc is warped originated from azimuthal variations in the scattered light surface brightness (Roberge et al. 2005). There are several published CO observations of TW Hya and we now compare these with the results of the modelling. Rosenfeld et al. (2012) studied the CO line wings in the inner ∼ 4 au of the TW Hya disc. They describe an excess of emission in the line wings which is fitted well by a model including a warped inner disc. However, the synthesized beam was > 90 au, precluding further comparison and the higher resolution channel maps published by Huang et al. (2018) show no obvious twist. Debes et al. (2017) and Poteet et al. (2018) measured the rotation of the optical surface brightness asymmetry from observations at 4 epochs. The rotation speed of the asymmetry led to the conclusion that there is an inner disc or warp within $r < 1$ au precessing on the timescale of 17 years. Such a feature is below the resolution of the CO observations described above. Teague & Foreman-Mackey (2018) tease out very small variations in the velocity field and CO brightness temperature, revealing a spiral. In the velocity residuals (their Fig. 4) there is an 'X' shape at $r < 0.2$ arcsec and this is indicative of non-Keplerian motion and consistent with a compact warp. Apart from the spiral, there is no further asymmetry discernible. If the shadowing were to affect the temperature in the disc, we would expect to see asymmetry in the molecular line emission. However, this effect is unlikely to be seen in the ^{12}CO line which originates in the lower density surface region of the disc (Casassus et al. 2019) and an analysis of ^{13}CO may be more informative. Molecules whose abundances are driven by radiative rather than thermal processes, such as HCO^+, may still present asymmetric emission (Young et al. 2021). Öberg et al. (2021) present DCO^+ observations in TW Hya. While there is no obvious asymmetry in the images, it would be worth searching for any small azimuthal variation that would be colocated with the location of the shadow at the time of observation. In summary, TW Hya is probably an example of a disc with a warp that is extremely difficult to detect because the angular scale of the warp is small and the misalignment is only very slight. In addition, the dust is depleted at the location of the possible warp or inner disc, which will further reduce the effect of shadowing.

4.4.2 HD 163296

In the simulated channel maps of a disc with a small warp, we see that the emission from opposite sides of the disc is slightly offset, especially in the central velocity channels, rather than being symmetrical as is the case for the aligned disc (see Fig. 12). The opposite sides of the disc in the channel maps of HD 163296 presented in Pinte et al. (2020) appear to be similarly offset from one another. This is separate to the 'kinks' identified by the authors which were attributed to planets. Previously, time-varying asymmetry has been observed in scattered light images (Rich et al. 2019), indicating time-variable illumination of the outer disc. A precessing inner disc and/or warp was posited to explain this. The larger scale asymmetry in the channel map would support the warp hypothesis. There may additionally be a very small precessing inner disc, like has been proposed for TW Hya, and this too would be accompanied by a warp.

4.4.3 Elias 2-27

The situation may be complicated when multiple effects are present. Paneque-Carreño et al. (2021) suggest that the Elias 2-27 disc is warped to explain the observed azimuthal asymmetry in the gas
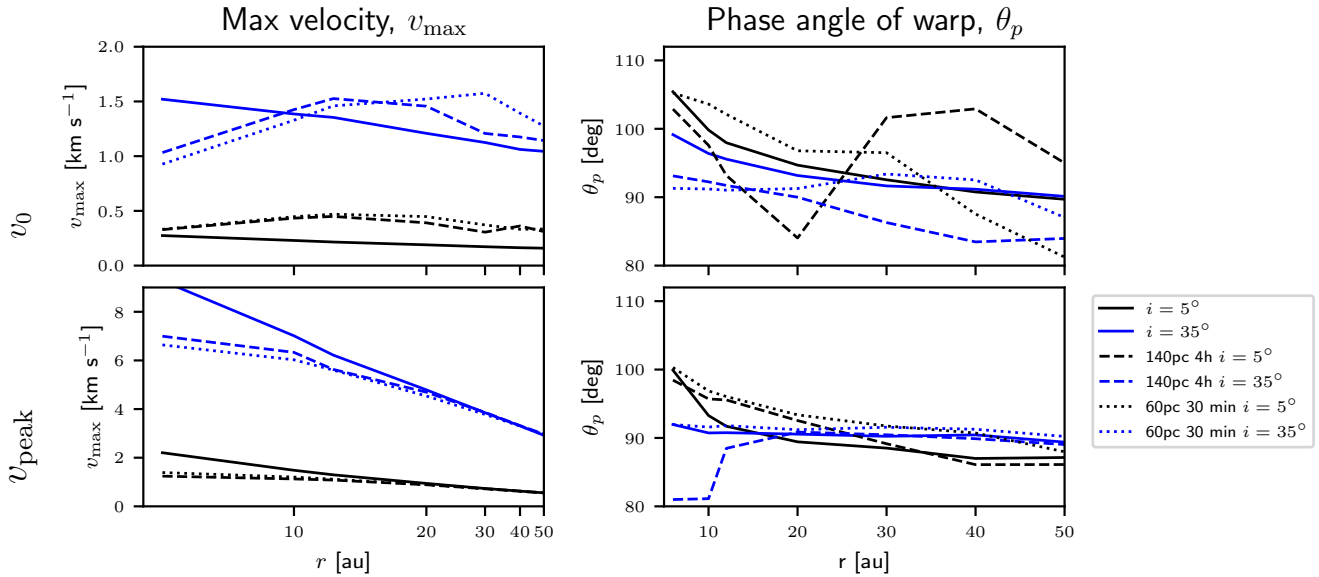
Figure 12. Continuum-subtracted channel maps for the 10° binary inclination model at various viewing inclinations and position angles (red shading). The corresponding channel maps of the aligned disc model are shown in grey (except panel f), reflected along the vertical axis for comparison to highlight the asymmetries in the emission from the warped disc. Panel g shows two channel maps from i=20, pa=180. Here we see asymmetry between opposite velocity channels. The back side of the disc is just detected at positive velocities (red) but not at negative velocities (grey).

the evidence has not been examined fully. Here we compare the predictions for the characteristic kinematic features of warped discs with three protoplanetary discs from the literature. As discussed earlier, the warp in our simulations is caused by a misaligned central binary but the structure is similar for warps resulting from various effects so the effects seen in line emission are also similar.

Figure 13. A comparison of the derived velocity and phase angle profiles from the synthesised CO data with added thermal noise and convolution with a Gaussian beam of 0.05 arcsec. The thermal noise was chosen to match the sensitivity of integration times of 4 hours and 30 minutes with the full ALMA array and we show the profiles from a distance of 140pc and from fluxes scaled to a distance of 60pc.

emission but the disc also hosts gravitational instability (GI) induced spirals (Pérez et al. 2016). Veronesi et al. (2021) also find Elias 2-27 to be susceptible to GI. The ^{13}CO velocity map presented by Paneque-Carreño et al. (2021) shows the same slight twist as in some of the velocity maps in Fig. 10. The residuals for the ^{13}CO and C^{18}O first moment maps of Elias 2-27 and the best fit model indicate a non-Keplerian velocity field. In appendix B, we examine the expected residuals from attempting to fit a Keplerian model to a warped disc further. We find the same features in the residuals that Paneque-Carreño et al. (2021) obtained from observations of Elias 2-27 (see Fig. B1), which strongly suggests this disc is warped. Late-stage infall onto the disc may result in both GI and warping so we may expect these two effects to occur simultaneously.

5 CONCLUSION

Many protoplanetary show signs of small misalignments through the shadows and asymmetric illumination seen in scattered light imagery. Through hydrodynamical and radiative transfer modelling of discs around misaligned binary systems, we have studied the effects of a small warp on the observed kinematics.

The key implications for identifying small warps in protoplanetary discs are as follows:

(i) The line profiles of warped discs are asymmetrical and velocities derived from observations are different to the intrinsic gas velocities. The quadratic method of determining the peak velocity field (Teague & Foreman-Mackey 2018) yields values closer to the intrinsic velocity than the standard first moment map. When noise is considered, this method still performs well, as long as the disc is resolved.

(ii) Keplerian fitting and subtraction does not necessarily produce an accurate velocity field. At worst, it produces spurious spiral arms and central features in the residuals when constant inclination and position angle are assumed across the whole disc.

(iii) The degree of observed warping can be quantified by extracting concentric annuli from the velocity map and fitting a sinusoid to each annulus. The 'twist' is then quantified as the change in position angle of the velocity peak with radius. This allows the detection of very small twists. Twists can also result from radial flows but for this model with a small warp the radial component of the gas velocity is $\lesssim 10^{-4}v_{Kep}$, which causes a shift in position angle $\ll 1°$ and has a negligible contribution to the twist in this case.

(iv) The greatest deviations are seen where the warp is strongest, in this case at $r < 20$ au. Observations must be suited to that scale for the best chance of detection. For example, the spatial resolution should be prioritised over spectral resolution in the case of a very compact warped region.

(v) Imperfect deprojection reduces the observed 'twist' and flattens the line-of-sight velocity radial profile making it more similar to that of an inclined, unwarped disc. The deprojection must be accurate to $\lesssim 5°$ to detect a small warp outside of the most strongly warped region through sinusoid fitting.

(vi) The velocity profiles of warped discs that are not close to face on are very difficult to distinguish from that of an unwarped disc since the contribution from the projected Keplerian motion dominates the velocity profile. The radius at which the warped disc velocity profile and the purely Keplerian profile become indistinguishable depends on the amplitude of the warp.

(vii) Like strongly warped discs, discs with small warps display the same twist in velocity maps. The observed twist depends on the optical depth and does not necessarily correspond to the true disc structure. Optically thin tracers provide better agreement with the disc structure.

(viii) At moderate viewing inclinations, the warp causes asymmetries in the CO channel maps out to 50 au, beyond where the amplitude of the warp is at a maximum. These features are distinct from those due to embedded planets ('kinks') and gravitational instability-induced spirals ('wiggles'). These effects were observed in models with a viewing inclination $i \lesssim 35°$ (Fig. 12, panel e.). The

shift in the location of the emission can be subtle and may have been missed in previous observations.

The kinematic detection of small warps is tricky but possible in most scenarios. Kinematic observations provide additional evidence of warping where a warp is suspected from scattered light observations or an alternative method when a source is too embedded for useful infra red observations. At low inclinations, CO observations can provide insight into the morphology of the warp and at moderate inclinations the warp causes detectable asymmetries in the channel maps. This provides a step towards the quantitative comparisons of observed warp structures with analytical and numerical models.

ACKNOWLEDGEMENTS

DATA AVAILABILITY

Hydrodynamical simulations used the PHANTOM code which is available from https://github.com/danieljprice/phantom. The input files for generating the SPH simulations and radiative transfer models will be shared on reasonable request to the corresponding author. Radiative transfer calculations were performed using MCFOST which is available on a collaborative basis from CP.

REFERENCES

Alencar S. H. P., et al., 2010, A&A, 519, A88
Astropy Collaboration et al., 2013, A&A, 558, A33
Barraza-Alfaro M., Flock M., Marino S., Pérez S., 2021, A&A, 653, A113
Bate M. R., 2018, MNRAS, 475, 5618
Bate M. R., Bonnell I. A., Price N. M., 1995, MNRAS, 277, 362
Benisty M., et al., 2017, A&A, 597, A42
Benisty M., et al., 2018, A&A, 619, A171
Casassus S., Pérez S., 2019, ApJ, 883, L41
Casassus S., et al., 2015, ApJ, 811, 92
Casassus S., Pérez S., Osses A., Marino S., 2019, MNRAS, 486, L58
Casassus S., et al., 2021, MNRAS, 507, 3789
Cuello N., et al., 2019, MNRAS, 483, 4114
Cullen L., Dehnen W., 2010, MNRAS, 408, 669
Debes J. H., et al., 2017, ApJ, 835, 205
Draine B. T., Lee H. M., 1984, ApJ, 285, 89
Esau C. F., Harries T. J., Bouvier J., 2014, MNRAS, 443, 1022
Facchini S., Juhász A., Lodato G., 2018, MNRAS, 473, 4459
Flaherty K. M., Hughes A. M., Rosenfeld K. A., Andrews S. M., Chiang E., Simon J. B., Kerzner S., Wilner D. J., 2015, ApJ, 813, 99
Flaherty K., et al., 2020, ApJ, 895, 109
Fragner M. M., Nelson R. P., 2010, A&A, 511, A77
Hall C., et al., 2020, ApJ, 904, 148
Harris C. R., et al., 2020, Nature, 585, 357
Huang J., et al., 2018, ApJ, 852, 122
Hunter, J. D. 2007, Computing in Science & Engineering, 9, 90
Juhász A., Facchini S., 2017, MNRAS, 466, 4053
Kraus S., et al., 2020, Science, 369, 1233
Laor A., Draine B. T., 1993, ApJ, 402, 441
Lesur G. R. J., 2021, A&A, 650, A35
Lodato G., Price D. J., 2010, MNRAS, 405, 1212
Lubow S. H., Martin R. G., 2018, MNRAS, 473, 3733
Lubow S. H., Ogilvie G. I., 2000, ApJ, 538, 326
Marino S., Perez S., Casassus S., 2015, ApJ, 798, L44
Mathis J. S., Rumpl W., Nordsieck K. H., 1977, ApJ, 217, 425
Muro-Arena G. A., et al., 2020, A&A, 635, A121
Nealon R., Dipierro G., Alexander R., Martin R. G., Nixon C., 2018, MNRAS, 481, 20
Nixon C., King A., Price D., 2013, MNRAS, 434, 1946
Öberg K. I., et al., 2021, AJ, 161, 38
Paneque-Carreño T., et al., 2021, ApJ, 914, 88
Papaloizou J. C. B., Lin D. N. C., 1995, ApJ, 438, 841
Papaloizou J. C. B., Pringle J. E., 1983, MNRAS, 202, 1181
Papaloizou J. C. B., Terquem C., 1995, MNRAS, 274, 987
Perez S., Dunhill A., Casassus S., Roman P., Szulágyi J., Flores C., Marino S., Montesinos M., 2015, ApJ, 811, L5
Pérez L. M., et al., 2016, Science, 353, 1519
Pérez S., Casassus S., Benítez-Llambay P., 2018a, MNRAS, 480, L12
Pérez L. M., et al., 2018b, ApJ, 869, L50
Pinte C., Ménard F., Duchêne G., Bastien P., 2006, A&A, 459, 797
Pinte C., Harries T. J., Min M., Watson A. M., Dullemond C. P., Woitke P., Ménard F., Durán-Rojas M. C., 2009, A&A, 498, 967
Pinte C., et al., 2018a, A&A, 609, A47
Pinte C., et al., 2018b, ApJ, 860, L13
Pinte C., et al., 2020, ApJ, 890, L9
Poteet C. A., et al., 2018, ApJ, 860, 115
Price D. J., 2007, Publ. Astron. Soc. Australia, 24, 159
Price-Whelan A. M., et al., 2018, AJ, 156, 123
Price D. J., et al., 2018a, Publications of the Astronomical Society of Australia, 35, e031
Price D. J., et al., 2018b, MNRAS, 477, 1270
Rich E. A., et al., 2019, ApJ, 875, 38
Roberge A., Weinberger A. J., Malumuth E. M., 2005, ApJ, 622, 1171
Rosenfeld K. A., et al., 2012, ApJ, 757, 129
Rosenfeld K. A., Andrews S. M., Wilner D. J., Kastner J. H., McClure M. K., 2013, ApJ, 775, 136
Rosenfeld K. A., Chiang E., Andrews S. M., 2014, ApJ, 782, 62
Shakura N. I., Sunyaev R. A., 1973, A&A, 24, 337
Siess L., Dufour E., Forestini M., 2000, A&A, 358, 593
Smallwood J. L., Lubow S. H., Franchini A., Martin R. G., 2019, MNRAS, 486, 2919
Teague R., 2019a, Research Notes of the American Astronomical Society, 3, 74
Teague R., 2019b, The Journal of Open Source Software, 4, 1220
Teague R., Foreman-Mackey D., 2018, Research Notes of the American Astronomical Society, 2, 173
Teague R., Bae J., Bergin E. A., Birnstiel T., Foreman-Mackey D., 2018, ApJ, 860, L12
Teague R., Bae J., Bergin E. A., 2019a, Nature, 574, 378
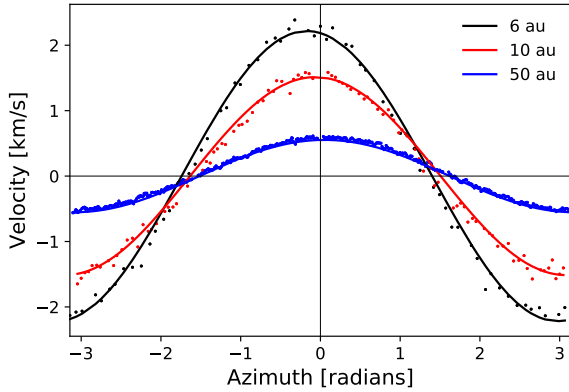Teague R., Bae J., Huang J., Bergin E. A., 2019b, ApJ, 884, L56

Figure A1. Velocity values extracted from annuli centered on three radii from the v_{peak} map of the 10° binary inclination model viewed at 5°. The curves are the resulting fits to the data points. The shift in position of the velocity peaks indicates the warp struture.

Terquem C., 2013, MNRAS, 435, 798

Terquem C., Bertout C., 1993, A&A, 274, 291

Veronesi B., Paneque-Carreño T., Lodato G., Testi L., Pérez L. M., Bertin G., Hall C., 2021, ApJ, 914, L27

Virtanen P., et al., 2020, Nature Methods, 17, 261

Weingartner J. C., Draine B. T., 2001, ApJ, 548, 296

Woods P. M., Willacy K., 2009, ApJ, 693, 1360

Xiang-Gruess M., Papaloizou J. C. B., 2013, MNRAS, 431, 1320

Young A. K., Alexander R., Walsh C., Nealon R., Booth A., Pinte C., 2021, MNRAS, 505, 4821

Zhu Z., 2019, MNRAS, 483, 4221

de Juan Ovelar M., Pinilla P., Min M., Dominik C., Birnstiel T., 2016, MNRAS, 459, L85

van Boekel R., et al., 2017, ApJ, 837, 132

APPENDIX A: SINUSOID FITTING

We fit sinusoids to annuli of the disc to analyse the velocity maps as described in section 3.3.1. Here, we briefly justify this choice and show examples. Fitting annuli required that the disc is viewed face on so that a given annulus traces regions at equal radii. For the velocity maps produced for a nonzero viewing inclination, we first deproject the maps. Fig. A1 shows an example of the pixel data extracted from a velocity map in three annuli and the sinusoids fitted.

We see that the warp is naturally revealed in the phase shift of the sinusoids. The amplitude of the sinusoid provides a reliable measure of the peak velocity because the contribution from all azimuths has the effect of averaging out the noise. The fit is only meaningful in the warped region. For example, in some of the synthetic velocity maps there is a wave propagating outwards beyond the warped region and an annulus would contain mainly either red- or blue-shifted emission. Some care must be taken then to check that a sinusoid is a good fit to the data.

APPENDIX B: KEPLERIAN FITTING WITH EDDY

Fitting a Keplerian disc model to a warped disc is naturally going to produce a poor fit. However, a warped region may only affect the inner few au of an otherwise near-Keplerian disc. It is also a ubiquitous method for analysing spectral line observations of circumstellar discs. We therefore attempted to fit some example velocity maps from our modelling with EDDY.
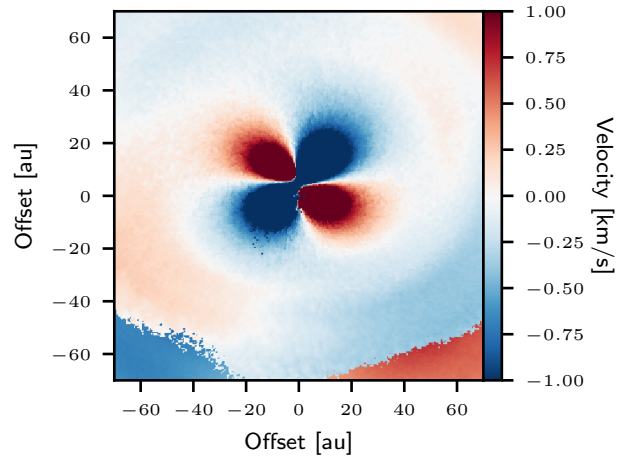

Figure B1. The residuals for the best fitting Keplerian model found with EDDY for the 10° binary inclination model with a viewing inclination of 35°.

The best fits were found by masking the inner region where the distortion was greatest and also by fixing the central mass and viewing inclination. An example of the residuals between the v_{peak} map and best fit model is shown in Fig. B1. For this example, the fitting was applied to the annulus with inner and outer radii 37 au and 67 au. The mass, distance, v_{lsr} and inclination were fixed to the simulation parameters: $2\,\text{M}_\odot$, 140 pc, $0\,\text{km}\,\text{s}^{-1}$ and 35° respectively. The central position and position angle were left as free parameters.

The residuals showed remarkably similar features for all inclinations 5-35°. These comprise an 'X' shape in the centre and one or two spiral-like features just beyond. Paneque-Carreño et al. (2021) report this 'X' shape in the residuals form fitting Elias 2-27 with EDDY. This feature is the result of subtracting a Keplerian field from a warped velocity field. We suggest that these observations of Elias 2-27 are consistent with a central warp.

This paper has been typeset from a TEX/LATEX file prepared by the author.